Available online at www.sciencedirect.com
ScienceDirect
Acta Materialia 58 (2010) 6115–6124
Acta MATERIALIA
www.elsevier.com/locate/actamat

Spacing characterization in Al–Cu alloys directionally solidified under transient growth conditions

Morteza Amoorezaei *, Sebastian Gurevich, Nikolas Provatas

Department of Materials Science and Engineering, McMaster University, Hamilton, Ontario, Canada L8S4L7

Received 16 December 2009; received in revised form 9 June 2010; accepted 19 July 2010
Available online 16 August 2010

Abstract

We study spacing selection in directional solidification of Al–Cu alloys under transient growth conditions. New experimental results are presented which reveal that the mean dendritic spacing vs. solidification front speed exhibits plateau-like regions separated by regions of rapid change, consistent with previous experiments of Losert and co-workers. Quantitative phase-field simulations of directional solidification with dynamical growth conditions approximating those in the experiments confirm this behavior. The mechanism of this type of change in mean dendrite arm spacing is consistent with the notion that a driven periodically modulated interface must overcome an energy barrier before becoming unstable, in accord with a previous theory of Langer and co-workers.

Keywords: Directional solidification; Dendrite; History dependent; Phase field simulation; Transient state

1. Introduction

Solidification microstructure is the starting point of any casting operation. Dendritic spacing and morphology established during casting often sets the scales of the downstream microstructure during manufacturing of alloys. This is particularly true in emerging technologies such as twin belt casting, where a reduced amount of thermomechanical downstream processing reduces the possibility of modifying microstructure length scales from that determined at the time of solidification.

Predicting columnar microstructure in cast alloys has been traditionally studied in the context of Bridgeman-type directional solidification conditions. Most studies have focused on the problem of primary and secondary arm spacing in dendrite arrays of thin liquid films of organic alloys, directionally solidified under steady-state cooling conditions, i.e. a sample is pulled through a constant thermal gradient at a constant pulling speed. Careful experiments on steady-state directional solidification reveal a reproducible correlation between spacing and pulling speed [1,2]. Studies of steady-state directional solidification have developed so-called geometric models to relate spacing to solidification processing parameters such as the pulling speed V, thermal gradient G and the alloy concentration c_o.

In geometric theories of spacing selection the structure and mathematical form of the dendrite arms is first assumed and a subsequent consistency relation is derived for the arm spacing (also referred to as “wavelength” in the literature). The construction and assumptions that go into setting up the geometry of the dendrite array lead to at least one phenomenological parameter that is fit to match the theory onto specific experimental spacing selection data [3–5]. While useful in helping to elucidate some aspects of spacing selection, such theories lack the fundamental element of microstructure predictability: the ability to self-consistently predict the morphology of the structure they are trying to say anything about. It is also not clear how such theories hold up to a change of conditions away from those of the experiments they were constructed to model.

While steady-state directional solidification is an important academic paradigm, it is not a realistic representation

---

* Corresponding author.
E-mail address: amoorem@mcmaster.ca (M. Amoorezaei).

1359-6454/$36.00 © 2010 Acta Materialia Inc. Published by Elsevier Ltd. All rights reserved.
doi:10.1016/j.actamat.2010.07.029

of the conditions prevalent during industrial casting, which normally occurs under rapidly changing growth conditions. Near a chill surface or, indeed, throughout the entire sample thickness in the case of very thin strips, the thermal gradient and solidification speed are neither constant nor independent of each other. Recognizing this, several research groups have attempted to extend geometrical models to include unsteady-state processing conditions. For example, Garcia and co-workers [6] and Kirkaldy and co-workers [4] have attempted to link the spacing of dendrite arms to the cooling rate $\dot{q}$. Once again, as with any geometric theory, phenomenological parameters are introduced to fit the model with experiments, although in this case the fits are not as good as in the steady-state case.

The importance of transient thermal processing conditions in establishing as-cast microstructures has been apparent since the theoretical work of Warren and Langer [7,8] and the experimental studies of Losert and Huang [9,10] on alloys of succinonitrile (SCN). Warren and Langer performed an analysis on the stability of dendritic arrays [7,8] and predicted that they remain stable to period doubling instability over a range of pulling speeds, contrary to the predictions of any geometric theory, whether steady-state or transient. Losert et al. [10] later observed that under a gradual change in pulling speed the spacing remained stable over a range of pulling speeds, consistent with the Warren and Lager predictions. They also noted the presence of an abrupt discontinuous jump in spacing at a particular pulling speed, which could be attributed to period doubling, also consistent with the predictions of Warren and Langer. In turn, Huang et al. [9] showed that by changing the rate of the pulling speed it is possible to obtain different spacings for a given set of final growth conditions. These works suggested a band of available spacings rather than a unique selection.

The results in the literature seem to point to two extremes. Under steady-state conditions, i.e. $dV/dt = 0$, the dendrite arm spacing appears to scale as a power-law of the pulling speed V, a result at least borne out qualitatively by geometrical models and some experiments. On the other hand, under transient solidification conditions, dendrite spacing and structure seem to depend strongly on transient history and initial conditions, at least in the idealized setting of a linear stability analysis or for well controlled experimental SCN dendrite arrays. The lack of unified theory to explain both these regimes likely points to an incomplete picture of the fundamental physics underlying microstructure selection in solidification. It also points to the need for a robust theory and modelling formalism that predicts the evolution of dendritic morphologies self-consistently, as function of only the input material parameters and cooling conditions, steady-state or transient.

Phase-field theory has emerged in recent years as promising candidate of a fundamental and self-consistent theory for modelling solidification microstructures. The first simulations to test spacing vs. pulling speed in alloys date back to the work of Warren and Boettinger [11], who found a monotonic band of spacings vs. pulling speed. The small system size used, however, precluded a quantitative comparison with experiments. Nowadays the phase-field methodology has become more quantitative by "marrying" simulations of phase-field models in the so-called thin interface limit [12,13] with novel simulation techniques like adaptive mesh refinement [14]. A first step using phase-field models to quantitatively model spacing in directional solidification was taken by Greenwood et al. [15] in two dimensions and Dantzig et al. in three dimensions [16]. These works modelled steady-state directional solidification in SCN alloys and found very good agreement (in the two-dimensional (2-D) limit) with the 2-D steady-state spacing experiments. These studies suggested that, at least under steady-state (i.e. Bridgeman growth) conditions and one type of initial condition (morphologically noisy initial interface), there could be a single crossover scaling function interpolating between the two power-law spacing regimes seen experimentally and modelled semi-empirically by geometrical models.

Despite the success of phase-field modelling in predicting steady-state spacing, as well as other steady-state properties such as cell tip structure [17], the methodology has not been used systematically to explore spacing under transient solidification conditions. Indeed, the ability to model cell, dendrite and seaweed structure, kinetic and surface tension anisotropy, different mobility, different thermal conditions and different initial condition makes phase-field modelling an ideal theoretical test ground to explore transient spacing development and how it may relate to the steady structures.

This paper reports new experiments and simulations that study primary spacing selection in directionally solidified Al–Cu alloys cooled under transient conditions closely related to those encountered in strip casting of Al alloys. The transient thermal gradient and interface speed are measured and correlated to measured dendrite spacing. Our results are shown to be inconsistent with steady-state and transient geometric theories. Instead, they suggest that there exists nearly stable ranges of spacings vs. front speed, connected by rapid changes in spacing at particular interface velocities. We also present new 2-D phase-field simulations that support this experimental picture. Our results are discussed in the context of Langer's theory as applied to a statistical distribution of spacings rather than a single unique spacing. In order to manage the length of this paper, a sequel to this paper [18] further explores some of the theoretical implications of the phase-field simulations presented here, focusing in particular on the connection between the transient behavior reported in this work and the steady-state behavior previously reported.

2. Experimental procedure

As-received Al–0.34 wt.% Cu samples were used to study solidification microstructure evolution under transient cooling conditions. The experimental set-up is shown in Fig. 1. It consists of a cylindrical stainless steel crucible that is water jet cooled from below to promote upward solidification. The crucible is shielded by a cylindrical alumina insulation with a thickness of about 10 mm to prevent radial heat extraction. The inner, outer and bottom parts of the crucible are covered with a thin layer of sprayed boron nitride in order to reduce the heat extraction through the walls as well as to provide a more uniform chilling surface at the bottom. The pressure of the spray was chosen to be high to prevent the formation of bubbles at the water–chilling wall interface due to local vaporization.

The temperature was measured at different heights from the bottom with K-type nickel–chromium-based sheathed thermocouples that are tightened along a plate and are inserted into the melt through the top of the crucible, as shown in the figure. The diameter of the chilling surface was set to 50 mm (i.e. the bottom plate) and the thickness of the chilling surface to 3.5 mm. The large chilling diameter helps to reduce the influence of the thermocouples' diameter, about 1 mm, on the solidification process. A set of thermocouples were aligned in the axial (vertical) direction, starting 1 mm from the chilling surface and separated from each other by 1 mm. In order to ascertain the one-dimensionality of the heat flow in the vertical direction, an additional thermocouple was positioned 12 mm radially from the aligned thermocouples.

The output from the thermocouples was acquired through a NI SCXI-1600 data logger, the calibration of which was set at the melting point of pure aluminum and pure zinc. Before pouring the melt into the crucible, the crucible along with the surrounding insulation and the alloy were heated in the same furnace to a temperature of 1.1 times the liquidus temperature of the alloy, to compensate for the heat loss during the experiment.

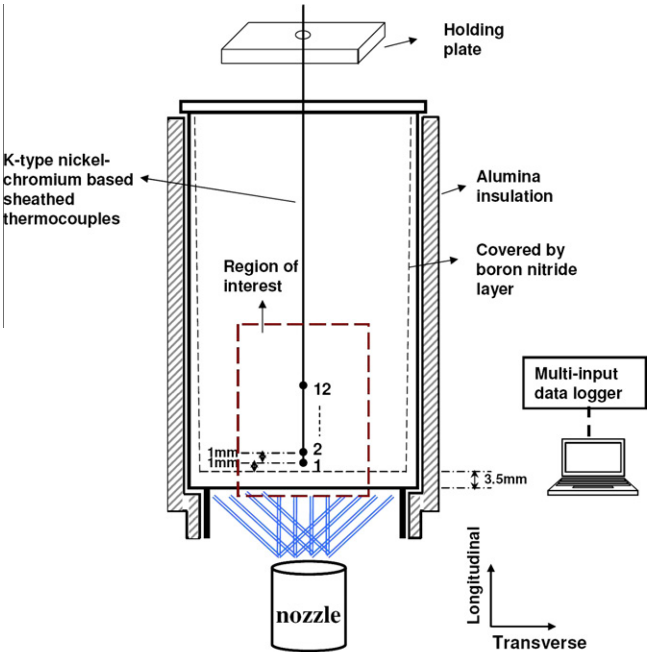

Fig. 1. Schematic of the set-up used to obtain upward directional solidification.

The cooling curves obtained from the thermocouples define a region of radially uniform temperature that varies essentially in the growth direction. This region is referred to as our region of interest. Outside this region, there is a small temperature gradient towards the wall such that the unidirectional heat flow breaks down. Far from the bottom chilling plate, outside the region of interest, the solidification microstructure mostly consists of equiaxed dendrites. Within our region of interest the solidification microstructure is columnar in nature (i.e. oriented cells or dendrites). We disregard any data outside our region of interest. As will be shown below, the grains examined within the region of interest are large enough in the direction transverse to the heat flow to disregard boundary effects. Only data from grains with transverse size larger than 1 mm are reported here. In each sample solidified, three different directionally solidified grains emanating from the chill surface were analyzed for reproducibility and to provide statistical error bars we report in our results.

Fig. 2 shows the longitudinal morphology of the dendrite microstructure cut out from a grain in one of our samples. The microstructure appears cellular in nature, while there is some evidence of side branching on the right of the figure, indicating the emergence of dendritic fingers. The microstructural length scale in the direction transverse to that of the heat flow (right to left in the figure) was analyzed statistically at different distances from the chilling surface using power spectral analysis. A typical power spectrum is shown in the bottom frame of Fig. 2. The x-axis of the power spectrum denotes the frequency of the corresponding wave vector. The main peak is associated to the primary spacing and is consistent with what is obtained by the ASTM line intersection method. The smaller frequency peaks correspond to fluctuations of primary variations away from the average, as well as smaller features, such as tip splitting and pixelation. The long wavelength variations correspond to feature variations larger than the mean, including finite size effects. We disregard wavelengths corresponding to such finite size effects in our analysis.

Fig. 3 shows a typical image of the corresponding transverse microstructure, cut away from a grain at distance 15 mm from the chilling surface. The bottom left frame of Fig. 3 shows the 2-D power spectrum averaged over three grains cut at the same position as the one in the top frame. The power spectrum was then circularly averaged about the origin, leading to an effective 1-D power spectrum, represented in the bottom right frame. Since the transverse microstructure is essentially isotropic, the position of the peaks does not shift after averaging. We applied this method to analyze our experimental data so that we can compare the 3-D experimental data as closely as possible to the way we analyze our 2-D simulations. The measure of dendrite spacing in this work is defined as $\lambda \equiv \sum_k k f(k)$, where $f(k)$ is a probability density of find-

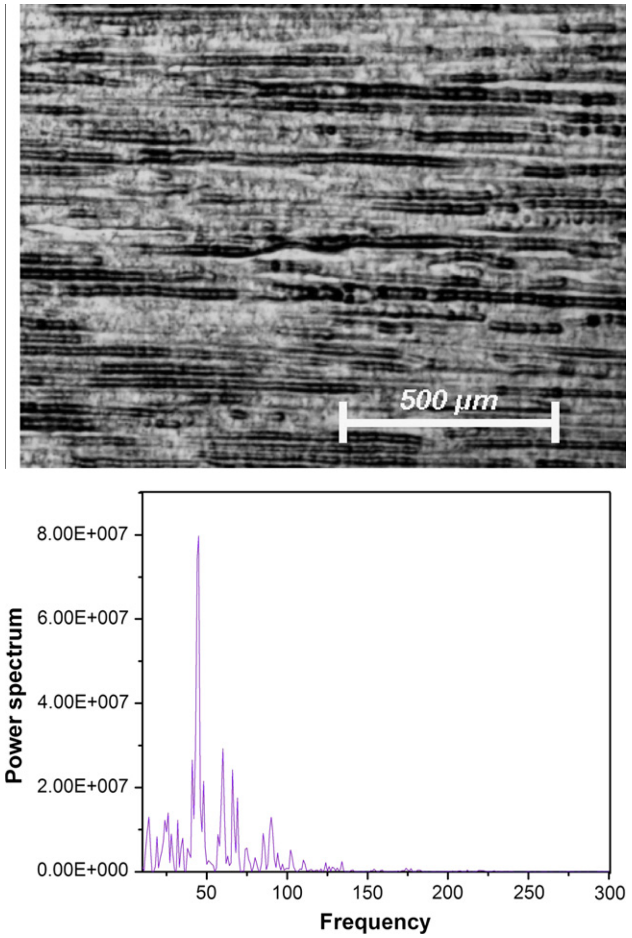

Fig. 2. (Top) Cutaway of the longitudinal solidification microstructure, growing from left to right. (Bottom) Unidimensional power spectrum of a transverse cut extracted from the longitudinal microstructure at a position 13 mm from the chilling surface.

ing features between the wavevector $k \rightarrow k + dk$, and is related to the power spectrum by $f(k) = P(k)/\sum_k P(k)$. In the analysis, the first nine wavevectors were discarded as these were noted to correspond to features on the scale of the system size.

3. Phase-field modelling

Phase-field simulations modelled solidification of the Al–Cu alloy system in the dilute limit of the phase diagram, which comprises straight solidus and liquidus lines of slopes of m/k and m, respectively. The equilibrium interface concentration jump at any temperature is thus given by partition relation $c_s = kc_l$, where c_s (c_l) is the molar concentration of impurities at the solid (liquid) side of the interface and k is the partition coefficient.

Simulations formally neglected the latent heat by imposing the temperature field by the form $T(z,t) = T_0 + G(t)(z - z_0 - \int_0^t V_p(t')dt')$, where $T(z_0, 0) = T_0$, a reference temperature, while $G(t)$ and $V_p(t)$ are the local thermal gradient and pulling speed, respectively. These were extracted from our experiments as discussed further below. We ignored convection in the liquid, as the transport of impurities becomes governed essentially entirely by diffusion [19]. Moreover, since diffusion of impurities in the solid is typically several orders of magnitude lower than in the liquid, diffusion in the solid was ignored.

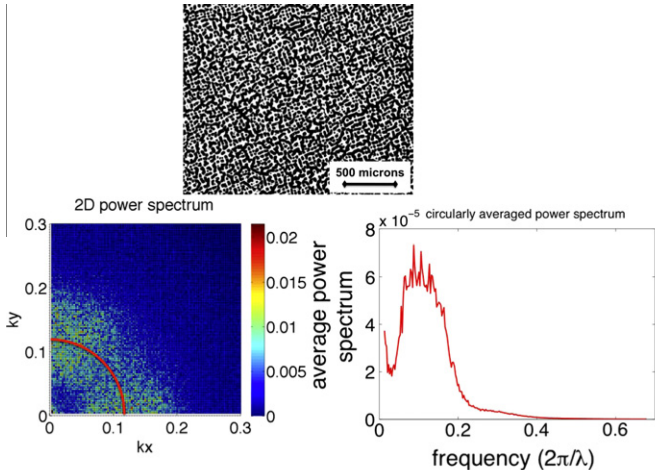

Fig. 3. (Top) Typical cross-section of transverse dendrite microstructure. (Bottom left) 2-D power spectrum averaged over three grains cut at the same transverse position as the grain in the top frame. The red curve corresponds to the mean wavelength obtained from the bottom right plot. (Bottom right) Circularly averaged power spectrum of the 2-D power spectrum in the bottom left frame. (For interpretation of the references to color in this figure legend, the reader is referred to the web version of this article.)

Under the above assumptions, mass conservation across the interface takes the form $c_l(1-k)v_n = -D\partial_n c|_l$, where D is the solute diffusion coefficient in the liquid and $\partial_n|_l$ is the partial derivative in the direction normal to the interface, taken on the liquid side. The temperature at the interface, which is assumed to be in local equilibrium, is given by the Gibbs–Thomson relation $T = T_m - |m|c_l - \Gamma\kappa - v_n/\mu_k$, where T_m is the melting temperature of the pure material, $\Gamma = \gamma T_m/L$ is the Gibbs–Thomson coefficient, γ is the interfacial free energy, L the latent heat of fusion per volume, κ is the interface curvature, v_n is the normal interface velocity and μ_k is the atomic mobility at the interface.

The underlying crystalline structure that defines the anisotropy of surface tension (or interface mobility) is modelled by through a commonly used fourfold symmetry anisotropy function $a(\hat{n}) = 1 - 3\epsilon + 4\epsilon\left(\hat{n}_x^4 + \hat{n}_y^4 + \hat{n}_z^4\right)$, where ϵ is the anisotropy strength and $\hat{n}$ is the unit normal at the interface. In two dimensions this function can be rewritten as $a(\theta) = 1 - \epsilon cos(4\theta)$, where θ is the angle between the normal direction to the interface and an underlying crystalline axis (e.g $\langle 1 0 0 \rangle$ in a cubic crystal).

Taking as reference the concentration on the liquid side of the interface $c_l^0 = c_0/k$ (where c_0 is the average alloy concentration), the following standard one-sided sharp interface directional solidification kinetics are modelled:

$$\partial_t c = D\nabla^2 c \quad (1)$$

$$c_l(1-k)v_n = -D\partial_n c|_l \quad (2)$$

$$c_l/c_l^0 = 1-(1-k)\kappa d_0 a(\hat{n}) - (1-k)\left(z-\int_0^t V_p(t')dt'\right)/l_T - (1-k)\beta v_n \tag{3}$$

where $d_0 = \Gamma/\Delta T_0$ is the solutal capillarity length, $\Delta T_0 = |m|(1-k)c_l^0$ is the freezing range, $l_T = \Delta T_0/G$ is the thermal length and $\beta = 1/(\mu_k \Delta T_0)$ is the kinetic coefficient.

The phase-field model employed to emulate Eqs. (1)–(3) is designed for quantitative simulations through the use of a thin interface analysis developed by Karma and co-workers [12,13]. This analysis makes it possible to emulate a specified capillary length and kinetic coefficient to second-order accuracy in the ratio of the interface width to capillary length. The details of this model have been presented and discussed at length in Refs. [12,13], thus only a brief description is included below. A general review of the phase-field method can be found in [20,16].

A scalar phase-field parameter ϕ is employed, which takes on a constant value in each phase and varies sharply but smoothly across a diffuse interface. The phase-field is used to interpolate the free energy density and mobility between the bulk phases. Its equation of motion guarantees the system evolves towards a minimum of the free energy of the system. We define a phase-field variable which takes the value $\phi = 1$ ($\phi = -1$) in the solid (liquid). The concentration $c(\vec{x}, t)$ is characterized through a generalization of the field $\widetilde{U} = (c - c_l^0)/(c_l^0(1-k))$, which represents the local supersaturation with respect to the point (c_l^0, T_0), measured in units of the equilibrium concentration gap at that temperature. This generalized supersaturation field is given by

$$U = \frac{1}{1-k}\left(\frac{c/c_l^0}{(1-\phi)/2 + k(1+\phi)/2} - 1\right) \tag{4}$$

In term of the fields c, ϕ and U, the phase-field model referred to above is given by

$$\tau(\hat{n})\left(1-(1-k)\frac{(z-z_{\text{int}})}{l_T}\right)\frac{\partial\phi}{\partial t} = w_0^2\vec{\nabla}[a(\hat{n})^2\vec{\nabla}\phi] + \phi - \phi^3 - \lambda(1-\phi^2)^2\left(U + \frac{z-z_{\text{int}}}{l_T}\right) \tag{5}$$

$$\left(\frac{1+k}{2} - \frac{1-k}{2}\phi\right)\frac{\partial U}{\partial t} = \vec{\nabla}\left[q(\phi)D\vec{\nabla}U - \alpha w_0(1+(1-k)U)\hat{n}\frac{\partial\phi}{\partial t}\right] + \left(\frac{1+(1-k)U}{2}\right)\frac{\partial\phi}{\partial t} \tag{6}$$

where $z_{\text{int}} \equiv \int_0^t V_p dt'$ is the interface position, $\hat{n} \equiv -(\vec{\nabla}\phi)/(|\vec{\nabla}\phi|)$ defines the unit vector normal to the interface, $\tau(\hat{n}) = \tau_0 \cdot a^2(\hat{n})$ is the phase-field orientation dependent relaxation time and $a(\hat{n}) = 1 - 3\epsilon + 4\epsilon[(\partial_x\phi)^4 + (\partial_z\phi)^4]$ imposes a fourfold anisotropy with strength ϵ in two dimensions. The function $q(\phi) = (1-\phi)/2$ dictates how the diffusivity varies across the interface. The interface thickness is given by w_0, while λ is treated as the numerical convergence parameter of the model.

The parameters λ, w_o and τ_o are interrelated through the thin interface relations developed in Refs. [12,13] to map the above phase-field model onto Eqs. (1)–(3). Specifically, once a particular lambda is chosen, the thin interface relations establish a unique choice of w_0 and τ_0 such as to yield the same d_o and β in simulations. The aim is to choose a rather diffuse value of w_0 in order to expedite numerical efficiency. In this work, we assume the interface kinetics coefficient $\beta \approx 0$, to lowest order. This ability to quantitatively model the materials parameters β and d_0 is largely due to the term containing the constant α in Eq. (6). The term is called the so-called "antitrapping current", whose function is to self-consistently counter the spurious effects of an interface thickness that is artificially enlarged for practical purposes.

The material parameters employed represent an Al–Cu alloy and are presented in Table 1. We solve the phase-field equations using either a finite difference explicit Euler scheme on a uniform mesh or, for simulations on larger scale, with a new finite difference adaptive mesh algorithm that utilizes a data structure developed by Provatas and coworkers [14,21].

Fig. 4 shows an example of a typical sequence of directionally solidified dendrite arms growth under steady-state conditions, i.e. a constant thermal gradient ($G = 5$ K mm^{-1}) and pulling speed ($V_p = 10$ μm s^{-1}). In order to systematically study the evolution of interface structure, and, in particular, the selection of the columnar microstructure spacing, we also perform a power spectral analysis on simulated interface profiles using a Fast Fourier transform. An example of such evolution is also shown in Fig. 4. The mean wavelength associated with the dendrite spacing for the simulations was calculated from the power spectrum using the same formula as the experiments. It is noted that the emergence of a split in the main peak of the spectrum at the earlier stage reveals a long wavelength modulation of the dendrite tips that eventually leads to cell elimination and the emergence of a new mean spacing.

The phase-field model was primarily used to simulate transient cooling conditions relevant to the experimental situation described in Section 2. This was done by using the thermocouple data from the experiments to extract the local thermal gradient across the solid–liquid interface and the effective velocity of the solidification front, which

Table 1
Material parameters that define the samples employed. m is the liquidus slope, c_0 is the alloy composition, k is the partition coefficient, D is the diffusivity of impurities in the liquid, Γ is the Gibbs–Thomson constant and ϵ is the anisotropy strength.

$\lvert m\rvert$ (K/wt.%)	3.00
c_0 (wt.%)	0.34
k	0.15
D (μm^2 s^{-1})	3400
Γ (K μm)	0.10
ϵ	0.02

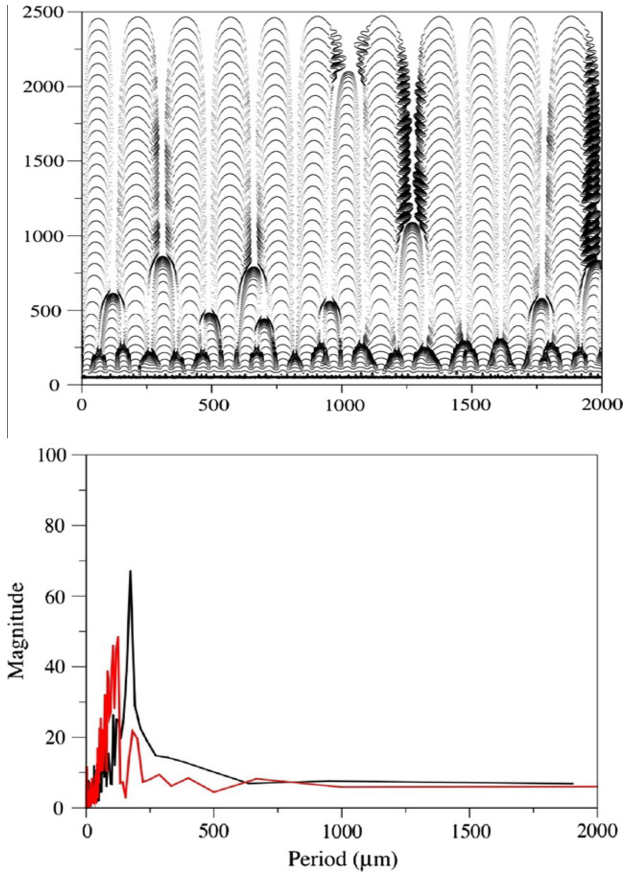

Fig. 4. (Top) An example of simulated evolution of a directionally solidified dendrite array grown under constant velocity and thermal gradient. The interface is initially morphologically noisy. Distances are in μm. (Bottom) Power spectrum of the last recorded interface structure (black line) as well as that of a close earlier time (red line). (For interpretation of the references to color in this figure legend, the reader is referred to the web version of this article.)

were then fitted to provide functions used to determine $G(t)$ and $V_p(t)$. The pulling speed was modelled after a fit of the front velocity obtained from experiments which, given that the interface is initially positioned at T_L (the liquidus temperature), is systematically lower than the actual front velocity, the discrepancy decreasing as the system evolves. Further details about this are discussed in Section 4.3.

Fig. 5 shows a typical spatiotemporal evolution of dendritic microstructures from our transient dynamic simulations. The morphological evolution has features in common with the experimental morphology in Fig. 2. Specifically, at early times, when the velocity is fastest, the morphology is cellular and then starts to exhibit some kinetically induced tip-splitting instabilities, giving rise to seaweed structures along the body of some primary stalks. We note that the kinetically induced tip splitting of primary tips is short-lived and occurs on length scales smaller than those controlling primary branch formation. They are thus expected to have only a minor effect on the evolution of the primary branch spacing, which is the main focus of this study. At slightly later times, dendritic primary arms with side branches emerge. The analysis of our phase-field simulations and the experimental data of Section 2 is discussed below.

4. Results and discussion

4.1. Finite size effects of grains

In order to avoid boundary effects on the dendrite arm spacing, we study arm spacing in as large a single grain as possible. The simulations, on the other hand, are more time consuming for larger systems. To estimate a convenient grain (or system) size to use experimentally and theoretically in our spacing selection analysis, we studied the dependence of dendrite spacing on the system size using phase-field simulations with constant control parameters. Fig. 6 shows the final steady-state spacing as a function of transverse system size (i.e. grain size) for four different pulling speeds. In all cases we started with a morphologically noisy interface.

These results indicate boundary effects become negligible at systems (grain sizes) larger than about 10^3 μm, even for the smallest rate of solidification, which leads to the largest spacing. The solidification rates studied experimentally and theoretically in the transient solidification analysis below are higher than those studied here, making finite size effects even more negligible in systems of 10^3 μm or larger.

4.2. Dendrite spacing evolution: experiments

Fig. 7 shows experimental (black curve) and simulated (red curve) plots of the transverse dendrite spacing as a function of the front velocity, which varies during solidification. In the experiments, the temperature gradient is coupled with the velocity and is not independent. The solidification rate is extracted from the cooling curves by considering that a thermocouple registers a sharp change in the temperature slope (with respect to time) when the solidification front passes through it. The experimental spacing shown is that obtained from transverse sections. Analysis of the longitudinal sections shows the same qualitative behavior, although the values are different, as expected. It is recalled that the experimental spacing data is obtained from different grains of the same experiment.

The experimental results in Fig. 7 are consistent with those reported by Losert et al. [10], as well as with older experiments of Huang et al. [22] on SCN. Namely, the spacing exhibits ranges of interface velocity where the spacing changes very slowly, between which it changes rapidly. It is noteworthy that the experimental data do not compare well quantitatively and, especially, qualitatively with the unsteady-state model of Hunt [23]. Plausible reasons for this will be addressed in Section 5.

Losert et al. associate a rapid change or jump in spacing at a particular velocity with a period doubling instability, as predicted by Warren and Langer, citing boundary effects to account for the discrepancy of the jump being less than a factor of two. For a small number of dendrite branches in a

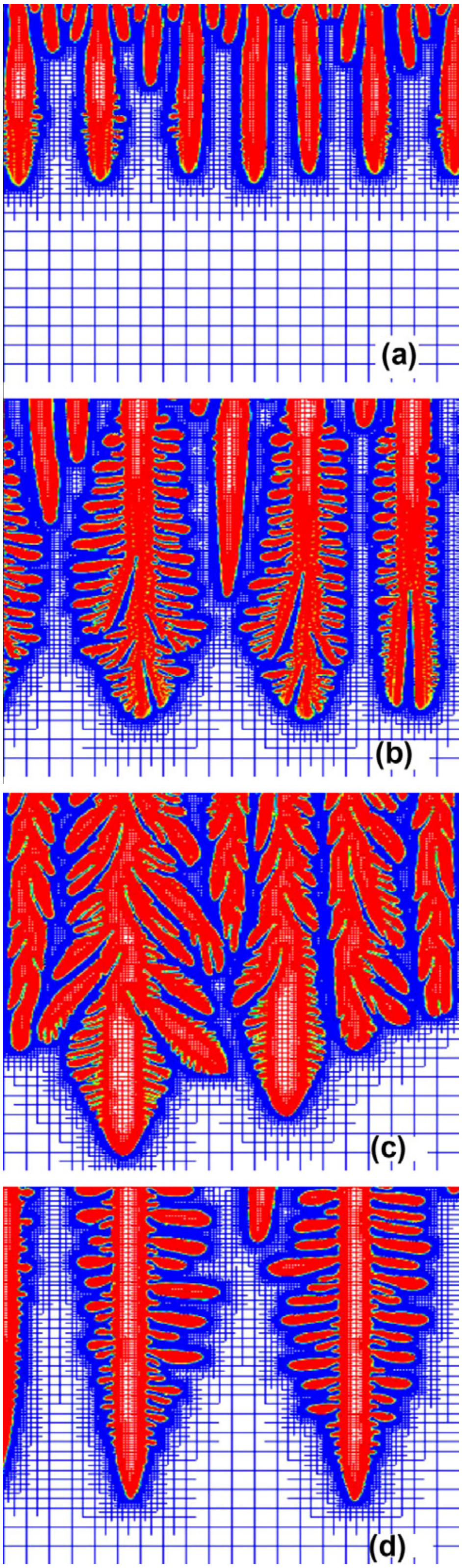

Fig. 5. Dendritic microstructure evolved during the PF simulation utilizing adaptive mesh refinement at the positions (a) 600, (b) 1200, (c) 3600 and (d) 11,400 μm from the initial position of the interface, corresponding to T_L. Each image is a zoom-in of the interface and is 65 μm in dimension. The color represents concentration. (For interpretation of the references to color in this figure legend, the reader is referred to the web version of this article.)

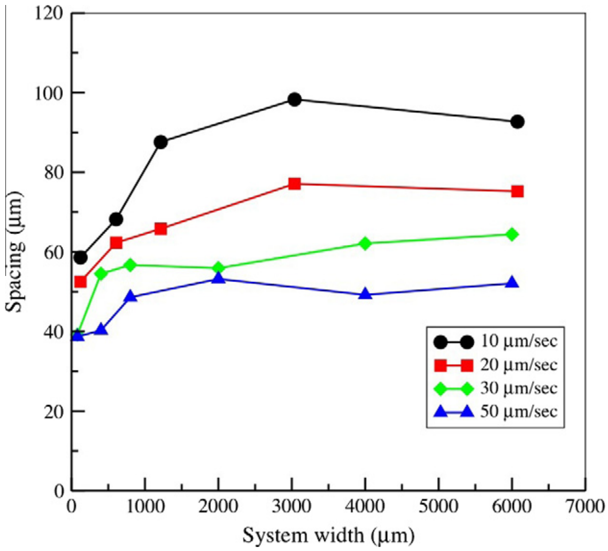

Fig. 6. Steady-state spacing vs. transverse sample width for different pulling speeds. The effect of the boundary becomes less prominent as the sample width increases. $G = 5\ \mathrm{K\ mm^{-1}}$.

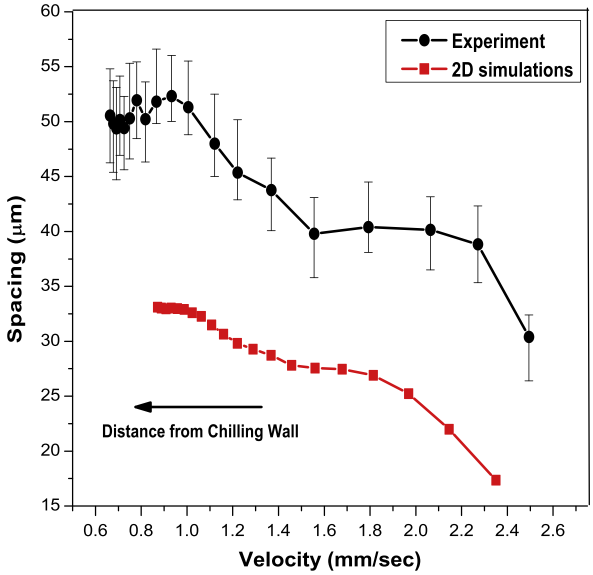

Fig. 7. Spacing as a function of velocity obtained experimentally (black curve) and numerically (red curve). Note that $G(t)$ is also dynamically changing at each point. (For interpretation of the references to color in this figure legend, the reader is referred to the web version of this article.)

system such as the one studied by Losert et al., the change in the spacing is sharp, i.e. the entire system can shift to a new wavelength almost simultaneously. The existence of such a jump can be associated with overcoming an energy barrier for a wavelength of a given spacing to become unstable and change (these barriers will be discussed further in Section 5). Conversely, for a large system comprising a distribution of wavelengths, the change in the mean spacing should exhibit a smoother evolution as not all wavelengths will satisfy the Warren and Langer instability criterion at the same time (i.e. at the same interface speed).

In this work, we study large systems comprising hundreds of dendrites and capture a distribution of wavelengths present in the system.

To support the above argument, Fig. 8 shows the 2-D power spectrum averaged over three grains, and the corresponding circularly averaged power spectrum for three different velocities in Fig. 7, namely, one in the lower plateau, one in the transition region and one in the higher plateau. The left plots in Fig. 8 indicate that the system does not contain a single wavelength, but rather a distribution of wavelengths centered about the mean. In the transition region, as the velocity decreases, some wavelengths will become unstable to period doubling (i.e. overcome the aforementioned energy barrier associated with that range of wavelengths), while the rest remain stable. Consequently, the mean spacing, defined as the average of the wavelengths, will change gradually rather than abruptly by virtue of sampling a distribution of wavelengths. This mechanism is also at work during the plateau region. In that case, the entire distribution of wavelengths is likely to be stable to period doubling or spacing change.

4.3. Dendrite spacing evolution: simulations

In order to approximate the growth conditions similar to those in our experiments, our directional solidification simulations included a variable thermal gradient and pulling speed, the values of which were set by fitting the corresponding curves obtained from experiments. Of course, the pulling speed is not the same as the front velocity, especially under transient effects, since the interface moves within the coexistence region as growth conditions vary. This discrepancy is largest during the early stages of the simulation due to the initial conditions.

The 2-D transient simulation data shown in Fig. 7 (red curve) show remarkably similar behavior to the experiments with regard to the step-like fashion in which the mean spacing changes with interface velocity. We also analyzed the behavior of the entire distribution of wavelengths in the simulated data and found that it changes with interface speed analogously to the experimental data in Fig. 8. It is noted that quantitative discrepancies between experiments and numerical results are to be expected due to the different growth conditions of the simulations compared to the experiments and that the simulations are two-dimensional. It is also noted that the initial interface conditions in simulations were different from those in experiments.

It is also noteworthy that the mean peak of the power spectra of the simulation data captures the main branch spacing and not the seaweed-like sub-structure evidenced in some of the branches of Fig. 5. The latter structures are present at early times and likely arise due to interface kinetics induced by the high solidification rate. Evidence of these structures also appear in the experimental data. Such tip-splitting instabilities may in fact play a role in establishing the initial interface conditions close to the chill wall in our experiments. To illustrate their emergence experimentally, we cooled a sample at very low rate for a short period of time an then increased the cooling rate abruptly. The resulting microstructure is shown in Fig. 9. At a low cooling rate, where the microstructure is larger, the microstructure comprises cellular branches. As the cooling rate is increased, it is clear that some of the new initial, finer spaced branches that emerge come about through tip splitting.

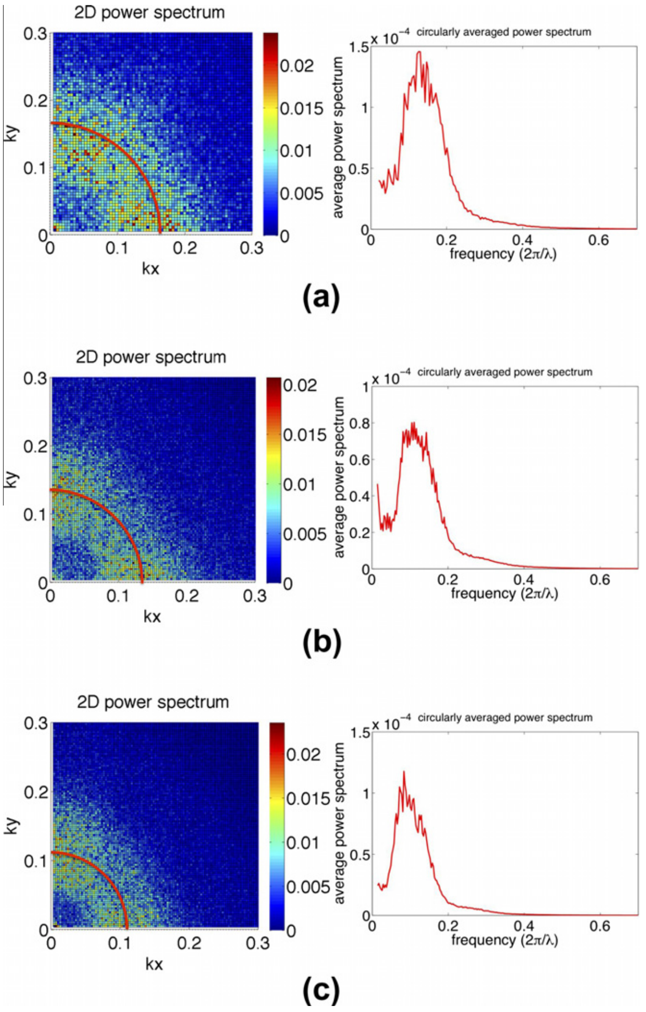

Fig. 8. (Left frames) 2-D power spectrum averaged over three grains and (right) the corresponding effective 1-D power spectrum of the transverse images at (a) 2500 μm (lower plateau), (b) 5800 μm (transition region) and (c) 10,000 μm (higher plateau) above the chilling wall. The red line in the left frames represent the mean spacing. (For interpretation of the references to color in this figure legend, the reader is referred to the web version of this article.)

5. Mechanisms for spacing plateaus

The existence of plateaus connected by rapid changes in spacing points to a dynamics in which an energy barrier has to be overcome for the spacing to adapt. Specifically, for the dendrite branch tip to split, it effectively needs to pass through a flattening stage in which the tip radius becomes effectively infinite. This lowers the interface undercooling (i.e. the contribution of dendrite tip curvature to interface undercooling, $d_0\kappa$, becomes zero), preventing tip splitting until a larger local interface velocity is reached. Increasing the velocity reduces the diffusion length and shortens the distance over which solute is rejected. This effect acts to reduce arm spacing. Hence, there will be a competition between the two effects, the first effect keeping the spacing stable until the driving force provided by second phenomenon is large enough to force dendrites or cells to split and reduce their spacing. Fig. 10 schematically represents the stages of tip splitting.

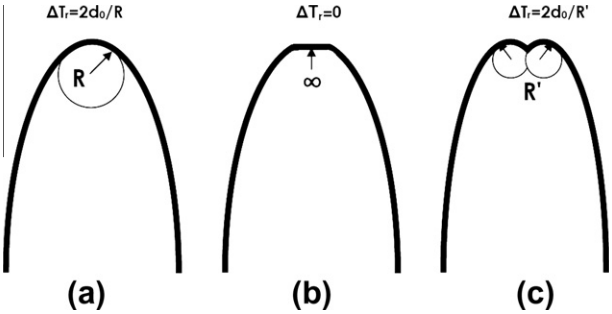

Fig. 10. Schematic representation of different stages during the tip-splitting mechanism. In the flattening stage (b), the undercooling due to the Gibbs–Thomson effect is essentially zero.

This effect of an energy barrier leads to the so-called “incubation time” used by Ma to describe the existence of plateaus in the transient directional solidification spacing data of Huang [22] using a geometrical model of transient solidification in SCN [24].

An increase in branch spacing via cell elimination occurs when a dendrite is blocked by either the secondary arms (in low speed solidification) of an adjacent dendrite or by the main stalk (in high speed solidification) of an adjacent dendrite. As shown in Fig. 11, in both cases, the seizing arm grows at an angle with a velocity component perpendicular to the growth direction of the primary arms (which is the direction of lowest energy, obtained as the product of anisotropy direction and heat flow direction). Unlike equiaxed growth, in directional solidification the growth rate of secondary branches is negligible compared to that of the main trunks. Thus, the seizing mechanism described above is not able to act until diffusion-mediated interactions through the melt become significant. As growth velocity decreases, solute diffuses a longer distance, and if the diffusion length of a dendrite is large enough, it interacts with adjacent diffusion fields. It is at this point that a jump in system energy can occur.

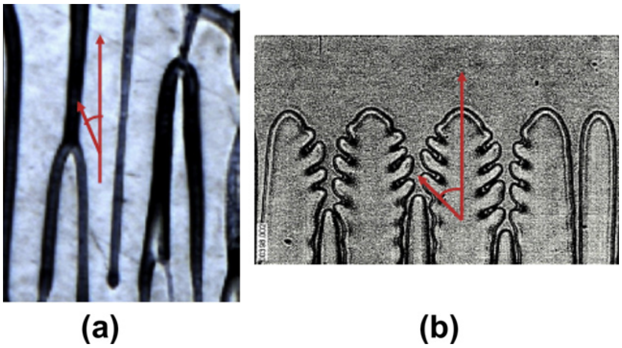

Fig. 11. Cell elimination caused by the neighboring (a) primary arms or (b) secondary arms [25] at high and low velocity solidification respectively.

In the case of cell elimination, there is an energy increase due to the growth in any of the undesired directions and an energy decrease for changes that increase the distance between dendrites (i.e. characterized by non-interacting diffusion fields). These two phenomena compete dynamically, with the spacing change eventually determined by the dominant effect, where the former effect acts as a barrier against the change in the spacing and the latter provides the driving force for cell elimination. It is also plausible that over a small range of cooling conditions (i.e. solidification rate, temperature gradient) these effects may balance each other, causing the spacing not to change very much, at least over some long-lived transient time (i.e. the plateau regions in the data). Furthermore, the farther from steady-state spacing the initial condition of the system, the higher the energy and the larger the driving force required for the system to perform branch elimination. Thus, it is possible that different spacings can also exist under the same cooling conditions, depending on the history of the system. Conversely, as the rate of change of the solidification front decreases, it is expected that the spacing vs. velocity should start to fall within a tight band of spacings for a given velocity. This connection between transient spacing selection and steady-state-type spacing is investigated in the sequel publication [18].

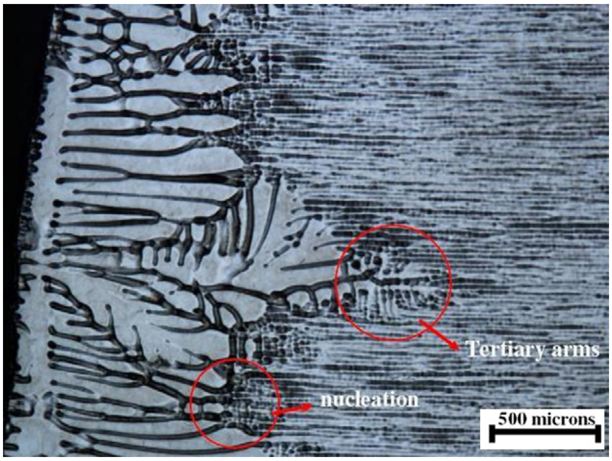

Fig. 9. Cast Al–Cu alloy showcasing the sharp change in morphology and spacing that occurs during a transition from a low cooling rate (large-scale structure) to a rapid cooling rate (finer structure).

Acknowledgements

We would like to thank the Canadian Space Agency (CSA), the National Science and Engineering Research Council of Canada (NSERC) and Novelis Global Technology Centre for financial support. We also thank Michael

Greenwood and Nana Ofori-Opoku for developing the adaptive mesh code, as well as Sumanth Shankar and David Montiel for the helpful discussions.

References

[1] Trivedi R. J Crystal Growth 1980;49(2):219–32.
[2] Bouchard D, Kirkaldy JS. Metall Mater Trans B 1996;27B(1):101–13.
[3] Somboonsuk K, Mason JT, Trivedi R. Metall Trans A 1983;15A(6):967–75.
[4] Bouchard D, Kirkaldy JS. Metall Mater Trans B 1997;28(4):651–63.
[5] Hunt JD. In: Solidification and casting of metals, vol. 3. London: The Metals Society; 1979.
[6] Cante MV, Spinelli JE, Ferreira IL, Cheung N, Garcia A. Metall Mater Trans A 2008;39A:1712–26.
[7] Warren JA, Langer JS. Phys Rev A 1990;42(6):3518–25.
[8] Warren JA, Langer JS. Phys Rev E 1993;47(4):2702–12.
[9] Lin X, Huang W, Feng J, Li T, Zhou Y. Acta Mater 1999;47(11):3271–80.
[10] Losert W, Shi BQ, Cummins HZ, Warren JA. Phys Rev Lett 1996;77(5):889–91.
[11] Boettinger WJ, Warren JA. J Crystal Growth 2000;200:583.
[12] Karma A. Phys Rev Lett 2001;87. 115701/1–4.
[13] Echebarria B, Folch R, Karma A, Plapp M. Phys Rev E 2004;70:061604.
[14] Provatas N, Goldenfeld N, Dantzig J. Phys Rev Lett 1998;80(15):3308.
[15] Greenwood M, Haataja M, Provatas N. Phys Rev Lett 2004;93(24). 246101/1–4.
[16] Provatas N, Greenwood M, Athreya B, Goldenfeld N, Dantzig J. Int J Modern Phys B 2005;19:4525.
[17] Gurevich S, Karma A, Plapp M, Trivedi R. Phys Rev E 2009; 80:1.
[18] Gurevich S, Amoorezaei M, Provatas N. Phys Rev E 2010, submitted for publication.
[19] Wang H, PhD thesis, McMaster University, Hamilton, ON; 2009.
[20] Boettinger WJ, Warren JA, Beckermann C, Karma A. Annu Rev Mater Res 2002;32:163.
[21] Athreya BP, Goldenfeld N, Dantzig JA, Greenwood M, Provatas N. Phys Rev E 2007;76(5). 056706/1–14.
[22] Huang WD, Geng XG, Zhou YH. J Crystal Growth 1993;193:105–15.
[23] Hunt JD, Lu SZ. Metall Mater Trans A 1996;27A(3):611–23.
[24] Ma D. Metall Mater Trans B 2002;33B:223.
[25] Private communications with W. Losert.